Journal of
Ceramic Science
and Technology

J. Ceram. Sci. Technol. 1-10 (2019)
DOI: 10.4416/JCST2019-00023
available online at: http://www.ceramic-science.com

Influence of the Printing Parameters on the Quality of Alumina Ceramics Shaped by UV-LCM Technology

P. Ożóg*[1, 2], G. Blugan[1], D. Kata[2], T. Graule[1]

[1]Laboratory for High Performance Ceramics, Empa, Überlandstrasse 129, 8600 Dübendorf, Switzerland
[2]Faculty of Materials Science and Ceramics, University of Science and Technology,
al. Adama Mickiewicza 30, 30 – 059 Cracow, Poland

received February 22, 2019; received in revised form July 6, 2019; accepted July 26, 2019

Abstract

The commercial alumina dispersion LithaLox HP500 from Lithoz (Austria) was 3D-shaped on a customized LCM device equipped with a light engine emitting at a wavelength of 365 nm and pixel size of 20 µm. The precision of the green part fabrication was measured using gear geometry and different exposure energies. The effect of the layer thickness on the shaping of the green bodies and the sintered ceramics was also evaluated. Additionally, the strength of parts fabricated using different layer thickness was tested in ball-on-three-balls testing and their fracture surfaces were analysed.

Keywords: Alumina, LCM, 3D printing, UV-curing, photopolymerisation

I. Introduction

A layer-by-layer fabrication approach is used in many Additive Manufacturing (AM) methods for ceramics. Layers are stacked together and each one has an individual pattern that corresponds to the object design [1]. There are many different AM techniques using such an approach [2–4], but here the authors want to mention only those based on photopolymerization; stereolithography (SLA) and digital light processing (DLP). In both techniques, suspensions undergoing photopolymerization are used to fabricate green bodies. Such solutions contain a ceramic powder dispersed in a photopolymerizable binder, which is a reactive monomer and/or oligomer; a dispersing agent and a photoinitiator are also used. Additionally, dispersions may contain a reactive or non-reactive diluent. The main difference between SLA and DLP lies in the layer curing. In SLA, a laser cures the pattern point-by-point, whereas in DLP the whole layer is cured all at once by a selectively masked light source (LEDs). That shortens the build time when several parts, even of various geometries, are fabricated during a single run. DLP has also the advantage of reduced oxygen inhibition effects as the suspension during polymerization is not directly exposed to air [3].

Currently, some commercially available systems for SLA and DLP can be found on the market. Fast Ceramics Production (FCP) is a solution developed by 3D Ceram Co (France) and is based on SLA. It was used, for example, to fabricate ceramic green bodies for zirconia dental crowns [5] and alumina parts [6]. In both cases, the ceramic pastes used were also developed by 3D Ceram Co 4, 5. The preparation of bone scaffolds for reconstructive surgery [7] is an additional example of using FCP technology.

Regarding DLP, there are some commercially available solutions for 3D manufacturing of ceramic materials: Large Area Maskless Photopolymerization (LAMP) technology was introduced by Georgia Tech spin-off DDM Systems (Georgia, USA) and was applied in the manufacturing of molds with integral cores for aerofoil investment casting [8]; ADMAFLEX is an AM technology developed by ADMATEC (Netherlands), which was used, for example, in studies on a custom one-piece dental implant 3D-shaped in yttria-stabilized zirconia dental material (TZ-3YS-E) [9] and Lithography-based Ceramic Manufacturing (LCM) is technology for ceramic materials which was initially developed at TU Vienna and further industrially developed by Lithoz GmbH (Austria) [10–12]. LCM seems to be the most commonly used of the aforementioned technologies [11–17].

Besides the available commercialized equipment for AM of ceramics, which is rather expensive, some groups have worked on developing their own low-cost equipment. An example is the work of Varghese *et al.* [18]. They developed a 3D printer using a DLP projector with a UV source emitting at a wavelength of 253 nm. Alumina and YSZ were fabricated in their study.

Schwentenwein *et al.* [19] published work in which an alumina slurry developed at Lithoz, LithaLox HP500 was 3D-shaped using a commercial CeraFab 7500 device from the same company. In their work, Lantada *et al.* [17] present capabilities and challenges of shaping using alumina slurry with the CeraFab 7500 with a pixel size of 40 x 40 µm at a wavelength of 460 nm.

* Corresponding author: paulinaozog90@gmail.com

In the current work, the same alumina dispersion was shaped using a custom-made unique CeraFab 7500 device, equipped with a light engine emitting at 365 nm wavelength and pixel size of 20 x 20 µm. The aim of this study was to evaluate the possibilities and limitations of the customized LCM device. Printing parameters such as exposure energy and layer thickness were modified to evaluate their effect on the *x-y* resolution, layer adhesion, and finally the flexural strength was tested with the ball-on-three-balls method.

II. Raw Materials

Commercially available alumina dispersion LithaLox HP500 from Lithoz (Austria) was used in this study to fabricate green bodies and study the 3D-structural shaping process on an LCM device equipped with a light engine emitting ultraviolet light. Normally, this slurry is used to form green bodies by performing photopolymerization process using blue light (about 460 nm wavelength).

This suspension contains 49 vol% high-purity alumina powder and has a density of 2.52 kg·m^3 [20], and (meth)acrylate monomers are used as a reactive binder [19]. Additionally, the dispersion contains proprietary non-reactive solvent, the dispersant and photoinitiators.

III. Processing and Shaping

The geometry of a gear was used to test the resolution of 3D shaping using a customized CeraFab 7500.A. *stl* file of a gear downloaded from *www.tracepartsonline.net* (Geradzahn-Stirnräder – Modul 0.5) and further modified using free freeware, *Autodesk® Tinkercad*™. Fig. 1 shows the gear geometry that was later fabricated.

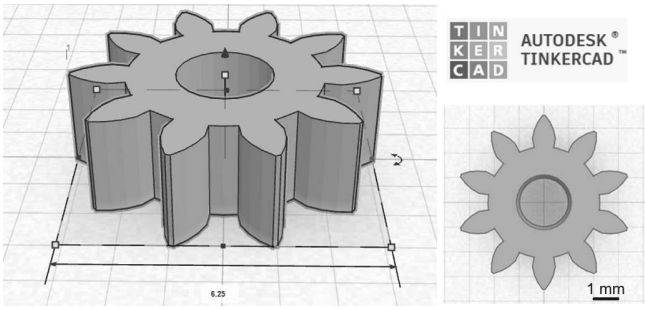

Fig. 1: Gear geometry with the outside diameter of 6.25 mm (representation in *Autodesk*"®" *Tinkercad*™; *https://www.tinkercad.com/)*.

The standard commercially available CeraFab 7500 device operates with a light engine emitting at wavelength of 460 nm. It has a lateral resolution of 40 µm (40 x 40 µm pixel size). That results in a building envelope of 76 mm x 43 mm in the *x-y*-axis and 150 mm in the *z*-dimension.

In this study, a custom-made unique CeraFab 7500 was used. It is equipped with a light engine which emits at 365 nm wavelength and it has better lateral resolution of 20 µm (20 x 20 µm pixel size). That results in a building envelope of 38 mm x 22 mm in the *x-y* dimension, and 170 mm in the *z*-axis. Layer thickness, being one of the printing parameters, can be modified in the range from 10 µm to 100 µm.

The range of exposure intensity which can be applied is different for the two light engines, based on light-emitting diodes (LEDs) and a digital micromirror device (DMD), mentioned above. The light engine emitting 365 nm wavelength can operate with exposure intensities in the range between 5 mW·cm^{-2} and 18.76 mW·cm^{-2}, whereas a range from 5 mW·cm^{-2} to 83.12 mW·cm^{-2} is obtainable for 460 nm LEDs. More details of the CeraFab 7500 working principle can be found in the relevant literature [19,21].

Various sets of printing parameters were used in the three-dimensional shaping process, in order to define those resulting in a geometry closest to the design. The printing parameters that were modified are presented in Table 1. In each case, 25 µm was the layer thickness being printed and five was the number of the starting layers. Those are the first five layers to which higher exposure energies were applied to improve adhesion between the building platform and the printed parts [18]. All the other parameters were maintained the same as recommended in the LithaLox HP500 data sheet [20]. Smaller gears were fabricated by applying scaling factors of 0.7 and 0.5 using *CeraFab DP* software, during preparation of the printing file.

In order to investigate the influence of the layer thickness on the green bodies and sintered ceramics, PP-5 and PP-6 were used and modified by changing the layer thickness to the values of 50; 75 and 100 µm. Green bodies of the gears were fabricated to perform this evaluation. Table 2 presents the printing parameters that were used.

Table 1: Printing parameters: exposure time.

Parameters	**PP-1**	**PP-2**	**PP-3**	**PP-4**	**PP-5**	**PP-6**
Layer thickness [µm]	25	25	25	25	25	25
Exposure time start [s]	6.40	5.86	5.1	3.2	1.6	1
Exposure time general [s]	5.87	5.33	4.80	2.93	1.2	1
Exposure intensity start [mW·cm^{-2}]	18.76	18.76	18.76	18.76	18.76	18.76
Exposure intensity general [mW·cm^{-2}]	18.76	18.76	18.76	18.76	18.76	18.76
Exposure energy start [mJ·cm^{-2}]	120.01	110.01	95.68	60.03	30.02	18.76
Exposure energy general [mJ·cm^{-2}]	110.01	100.01	90.01	55.04	22.51	18.76

Table 2: Printing parameters: layer thickness.

Parameters	PP-6	PP-7	PP-8	PP-9	PP-10
Layer thickness [μm]	25	50	75	75	100
Exposure time start [s]	1	1	1	1.6	1.6
Exposure time general [s]	1	1	1	1.2	1.2
Exposure intensity start [mW·cm^{-2}]	18.76	18.76	18.76	18.76	18.76
Exposure intensity general [mW·cm^{-2}]	18.76	18.76	18.76	18.76	18.76
Exposure energy start [mJ·cm^{-2}]	18.76	18.76	18.76	30.02	30.02
Exposure energy general [mJ·cm^{-2}]	18.76	18.76	18.76	22.51	22.51

The flexural strength of the specimens fabricated using the customized CeraFab 7500 was tested using the ball-on-three-balls (B3B) method. Specimens for the B3B tests were fabricated using PP-4 with different layer thicknesses in the shaping process: 25 μm, (type A), 50 μm (type B), 75 μm (type C) and 100 μm (type D). An. *stl* file of a 5.3-mm-diameter disc was used to manufacture the specimens.

Three-dimensionally shaped green bodies were debinded in air atmosphere according to the temperature programs provided by Lithoz in the data sheet with program parameters [22]. Debinding was performed at the maximum temperature of 900 °C in a PC 12 furnace from Pyrotec (Germany) and sintering at 1 600 °C for 2 h in air in a HTF 1700 furnace from Carbolite Gero (Germany). A graphical representation of both thermal treatment process temperature profiles is given in Fig. 2.

Fig. 2: a) Debinding and b) sintering profile of LithaLox HP 500 parts.

IV. Characterization Techniques

Green bodies fabricated on the LCM device and sintered parts were analyzed with a light microscope SteREO Discovery V20 from Carl Zeiss (Germany), in order to evaluate the presence of defects.

Density of the sintered ceramic pieces was measured using a Helium Pycnometer AccuPyc II 1340 from Micromeritics (USA). A value of 3.98 g·cm^{-3} [23] was used as a reference to calculate relative density.

Biaxial strength of specimens fabricated using different layer thickness was determined by means of B3B tests performed using a Zwick Z005 from Zwick/Roell (Germany) with a load cell of 200 N. Tests were carried out under relative humidity of 42.1 ± 3.3 % and temperature of 24.0 ± 0.4 °C. The load applied to the specimen was increased at the rate of 1 mm·min^{-1}, until failure occurred. Prior to the B3B test, the thickness and the diameter of the specimen were measured using a micrometer. Dimensions were measured three times for each specimen. Then the average specimen dimensions were calculated and used for the calculations. After the B3B test the average strength was calculated for each set of specimens, 3D-shaped using different layer thickness. Additionally, the average thickness for each specimen type was calculated and is given in Table 3.

The maximum load value at the moment of a fracture was used to calculate the strength of a specimen and the strength was calculated according to Eq. 1:

$$\sigma_{B3B} = f \cdot \frac{F}{t^2} \quad (1)$$

where σ_{B3B} is the flexural strength [MPa], F is the applied force at the moment of failure [N] and t is the thickness [mm] of the specimen. The dimensionless factor f depends on the ratio of the thickness to the disc radius. More details about the B3B test can be found elsewhere [24, 25]. The Weibull modulus was calculated according to the standard EN 843 – 5 [26].

The microstructure after sintering was examined with a scanning electron microscope (SEM), a Vega Plus 5136 MM from Tescan (Czech Republic), on as-sintered surfaces and on fracture surfaces. Before the microstructural investigations, the materials were not further polished or etched. The mean grain size of the sintered alumina was determined with the linear intercept method according to the standard EN 623 – 3:2001 [27]. Photos of four different areas were analyzed applying at least nine straight lines randomly oriented and measuring at least 200 intercepts using the LINCE software from TU Darmstadt (Germany). A correction factor of 1.56 was used for the calculations [28].

Table 3: Summary of B3B tests.

Specimen type	**A**	**B**	**C**	**D**
3D printing layer thickness [µm]	25	50	75	100
Number of tested specimens	28	32	45	29
Specimen thickness [mm]	0.42	0.42	0.39	0.39
Average strength [MPa]	483 ± 119	530 ± 74	487 ± 83	475 ± 80
Median strength [MPa]	529	532	456	480
Weibull modulus m [-]	6.0	6.6	4.9	5.6
Characteristic strength [MPa]	558	568	528	528
90% confidence band [MPa]	528 – 590	542 – 595	501 – 557	499 – 560

Image analysis was done using *Imagic ims Client* software from Imagic Bildverarbeitung AG (Switzerland). In the case of gears, the outside diameter and the gear hole diameter were measured five times and the average calculated.

V. Results and Discussion

(1) Effect of exposure energy

Printing parameters PP-1 and PP-2 correspond to the exposure energy range recommended in the dispersion data sheet of LithaLox HP500. Exposure energy ranges given in the slurry data sheet correspond to using the Lithoz device equipped with the light engine emitting wavelength of 460 nm. A photo of the green body obtained using PP-1 is shown in Fig. 3. The tips of the gear teeth are rounded instead of having sharp points. The gaps between the gear teeth are not present. Additionally, the gear hole is closed by polymerized film. That indicates that PP-1 causes overpolymerization of the dispersion.

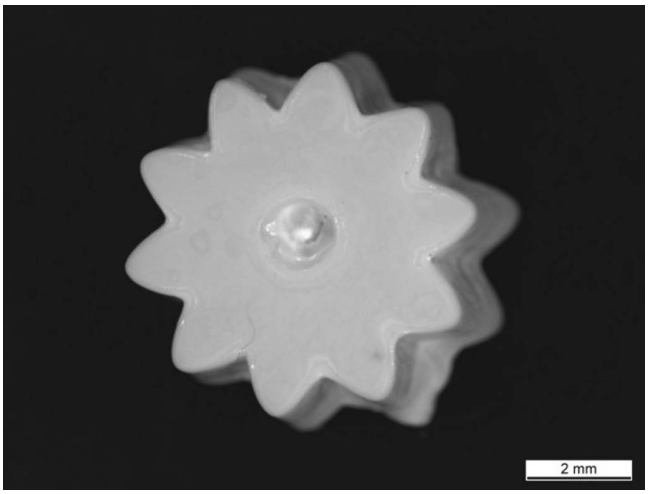

Fig. 3: Green body obtained using PP-1 (no scaling factor).

Reducing the exposure energy improves the resolution of the green bodies. Teeth tips become sharper; gear holes gradually open more in the case of gears of all sizes. Finally, only printing parameters PP-5 and PP-6 allowed fabrication of gears close to the geometry shown in Fig. 1 and with the best *x-y* resolution. Fig. 4 depicts photos of the gears three-dimensionally shaped using PP-6 and scaling factors of 1, 0.7 and 0.5.

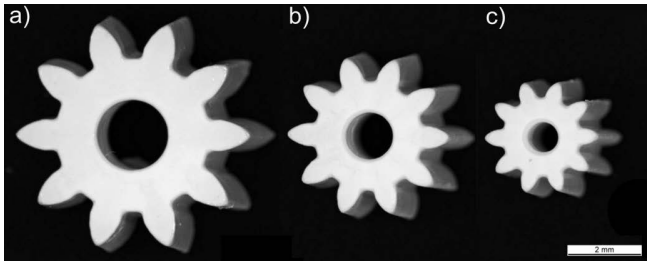

Fig. 4: Green bodies obtained using PP-6 a) no scaling, b) scaling 0.7, c) scaling 0.5.

The outer diameter of the gears is the closest to the value of 6.25 mm (*.stl* file) for the PP-5 and PP-6. However, when the dimensions of the gears fabricated using these two printing parameter sets are compared, no significant difference is observed. Yet, there is still some deviation from the. *stl* file dimensions. An overgrowth of 2.08 % and 0.68 % was recorded for the 3D gears printed using PP-5 and no scaling factor and scaling factor of 0.7 respectively. Gears with a scaling factor of 0.5 showed an undergrowth of 0.32 %. Applying PP-6 resulted in overgrowth values of 1.57 % and 0.22 % and an undergrowth value of 1.28 % for the gears with no scaling factor, 0.7 and 0.5 scaling factors being used respectively. Only in the case of the gears printed using scaling factor of 0.5 and parameters sets PP-5 and PP-6 was undergrowth observed. In the case of the gears shaped using the same scaling factor and the printing parameter sets PP-3 and PP-4, an overgrowth of 8.31 % and 4.15 % was observed respectively for the outside gear diameter.

As expected, using higher exposure energies resulted in more significant dimensional deviations from the original design, both in the case of the outer diameter and the gear hole. However, dimensional differences are higher for the diameter of the hole, independent of the printing parameters being applied. In the work by Mitteramskogler *et al.* [29], such dimensional deviations were observed, too, and light scattering was mentioned as their cause. According to Mitteramskogler *et al.* and on the basis of our own experience, the larger the component area surrounding the hole,

the more significant light scattering and overgrowth of the solidified dispersion are caused.

The light microscope observations of the sintered parts revealed the presence of defects. An example, the tooth of the gear printed using PP-4 is shown in Fig. 5a. The side surface of the gear is not completely smooth, and a few grooves can be observed (arrows), caused by specimen handling in the green state. Some lines defining the different layers (dash-dot line) can also be observed. Yet, they do not appear over the whole height of the part. Fig. 5b shows the part printed using PP-5. A line pattern is present on the part side and it seems to occur along the printed layers and only on the outer surface. One of the lines is darker than the others (dot line), suggesting that it penetrates inside the specimen. Additionally, some voids are observed. Similar features are observed in the case of the gear printed using PP-6 (Fig. 5c, dot and dash-dot lines). However, this specimen exhibits a higher number of the darker lines. The observed lines appear along the layers, suggesting that they may be cracks caused by delamination issues during 3D shaping [29].

(2) Layer thickness vs. layer adhesion

Printing parameters PP-6 were selected to be applied in investigating the effect of the layer thickness on the green body, by modifying the layer thickness. Using PP-6 illumination conditions, parts using a layer thickness of 25 and 50 μm could be manufactured. Using 75 μm as the layer thickness caused layer adhesion problems; it was not sufficient to keep the layers together. During fabrication some of layers separated from the ones already deposited on the building platform. They remained on the vat's surface and caused discontinuity of the recoated layer of slurry. Due to this fact, PP-5 was modified by increasing the layer thickness to 75 μm, giving PP-9. The associated increase in exposure energy was sufficient and allowed completion of the shaping process. PP-5 was modified further to PP-10 by increasing layer thickness to 100 μm. In this case, no adhesion issues occurred during shaping of the parts. Fig. 6 shows the teeth of the gears in the green state fabricated using 50; 75 and 100 μm layer thickness.

Layer thickness above 25 μm resulted in a formation of a line pattern along the layers. Using 50 μm as the layer thickness resulted in specimens not exhibiting any layer cohesion issues. However, the edges of the gear teeth are uneven (Fig. 6a, dash-dot line). Parts shaped using a layer thickness of 75 μm resulted in a crinkle-cut-like side-surface finish (Fig. 6b, dash-dot line). Using a layer thickness of 100 μm caused pronounced delamination problems (Fig. 6c, dash-dot line) and a side-surface finish similar to that obtained when a 75 μm was used as the layer thickness.

Fig. 7 shows the side view of the sintered gears. They were 3D-fabricated using a scaling factor of 0.7 and layer thickness of 25 μm (Fig. 7a), 50 μm (Fig. 7b), 75 μm (Fig. 7c) and 100 μm (Fig. 7d). A light source was used to identify the presence of defects in the sintered gears.

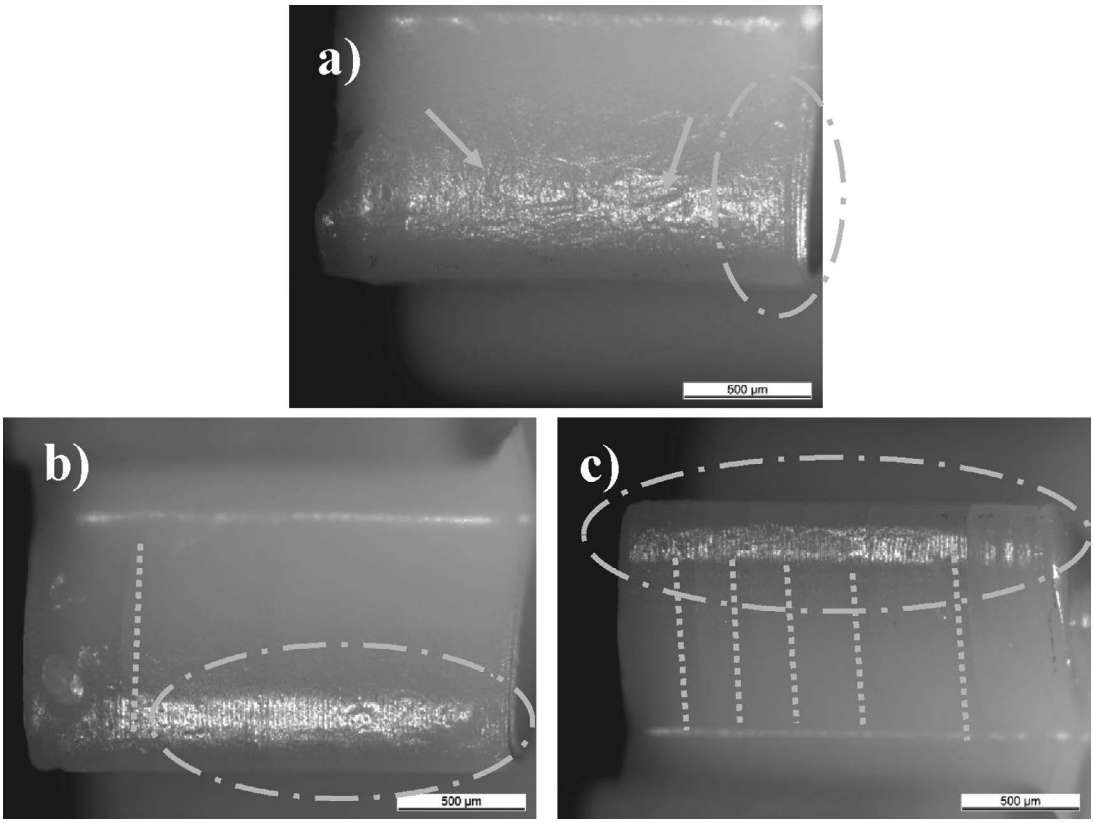

Fig. 5: Teeth of the sintered gears printed using a) PP-4; b) PP-5; c) PP-6.

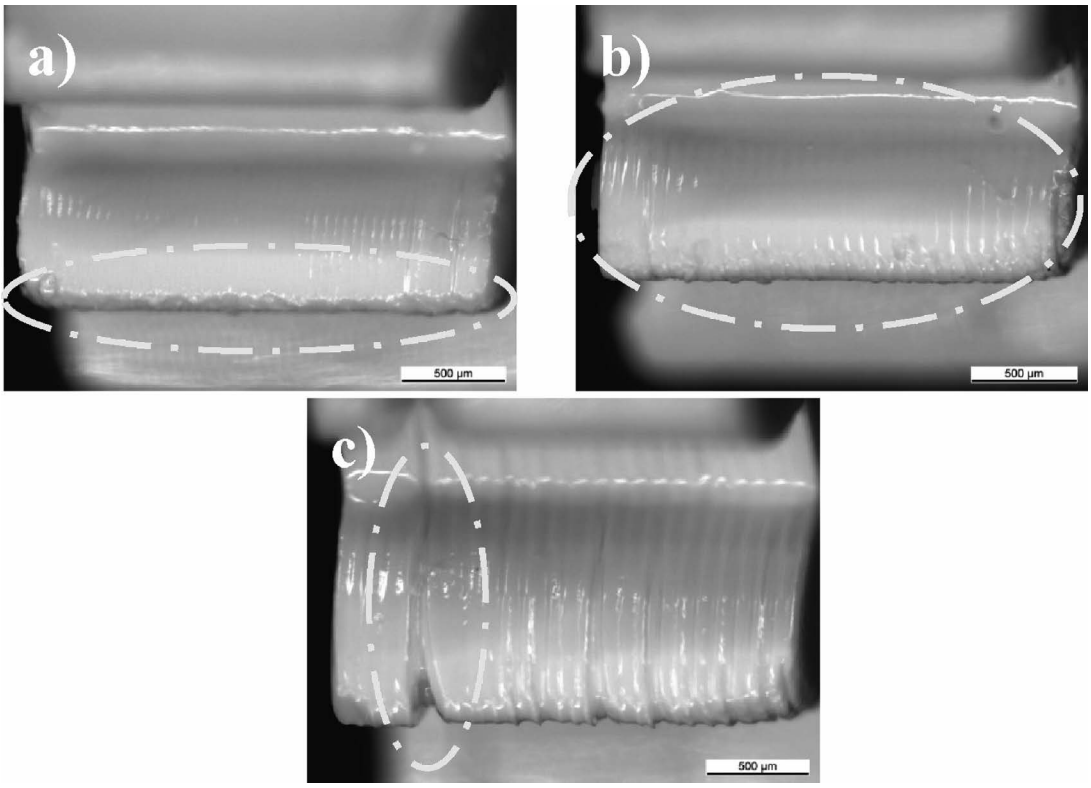

Fig. 6: Gear teeth in green state with the layer thickness of a) 50 µm; b) 75 µm; c) 100 µm.

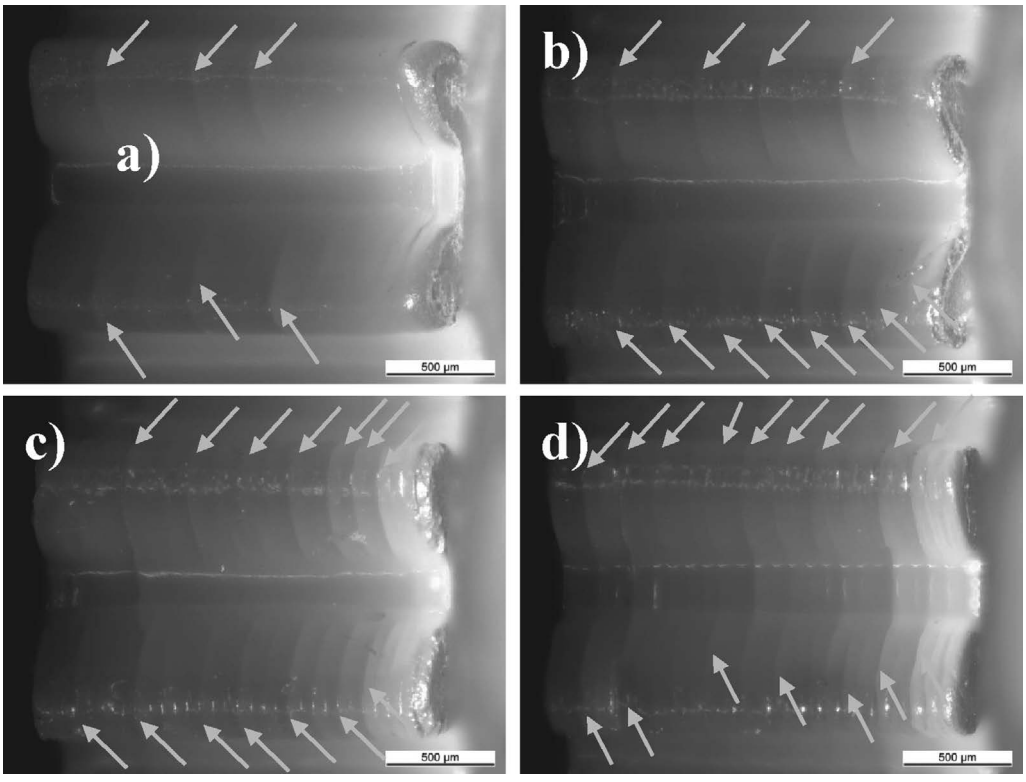

Fig. 7: Sintered gear teeth, layer thickness of a) 25 µm; b) 50 µm; b) 75 µm; c) 100 µm.

A lot of dark lines occurring along the layers can be seen. Lines indicate the presence of cracks in the specimens (Fig. 7, arrows). That means some layer adhesion issues appeared already during the shaping stage [29]. Parts manufactured using 25 µm do not have as many cracks as the specimens fabricated using higher layer thickness. Three-dimensionally manufactured specimens using 100 µm as the layer thickness have cracks that appear every two to three layers. Some of the cracks are present along a part of a layer, especially in the gear teeth, this is visible in the parts 3D-shaped using 25 µm, 50 µm and 75 µm. In the case of a layer thickness of 100 µm, cracks are present along the

whole layer. The cure depth being insufficient to provide good layer adhesion at the applied exposure energies (see Table 2) is an explanation of the observed phenomenon.

In order to avoid any layer adhesion problems in the green bodies and crack formation in the sintered pieces, it is recommended that a dispersion cure depth evaluation is performed prior to the 3D shaping process. Then adequate exposure energy can be adjusted for the particular layer thickness. However, a compromise has to be found between exposure energy resulting in good layer adhesion, side-wall surface finish and the dimensional feature resolution. In this case, none of the printing parameters used (PP-6, -7; -8;. 9; -10) meet that compromise. Therefore, exposure energy in the range between 30 mJ·cm^{-2} and 50 mJ·cm^{-2} should be used.

(3) Mechanical testing and fractography

All the specimens tested with the B3B method were as-sintered. The specimens had a tendency to break in to 2 – 3 pieces. The energy stored at the moment of failure defines the number of pieces a specimen breaks into. The higher that energy is, the more pieces will be created on specimen failure [28]. Some of the specimens did not break into pieces, but crack lines could be observed in the specimen; one of A-type, one of B-type, thirteen of C-type and thirteen of D-type. A few specimens showed behavior indicating slipping away from the measurement set-up during application of a low load. It was observed for two of type-A; one of type-B; four of type-C and two of type-D specimens. That occurred probably due to the fact that specimens were not completely flat. Some of the investigated specimens broke already at pre-loading stage; one of type A, two of type D. Therefore, the number of the tested specimens is different than the number of specimens prepared for the B3B tests. Results of the B3B tests are summarized in Table 3. Specimens of A type have relative density of 96 %, type B of 97 %, type C of 97 % and type D of 98 %.

The highest average strength value of 530 MPa was observed for B-type specimens. However, A- and B-type specimens exhibit similar mean strength values, which are higher compared to those of C- and D-type specimens. Within a batch of each specimen type, the lowest strength values were measured for the specimens which "slipped away" during the test e.g. specimen 26-A type had a strength of 203 MPa, specimen 3-B type had a strength of 265 MPa, specimen 13-C type had a strength of 223 MPa and specimen 1-D type exhibited a strength of 335 MPa. Those specimens did not break during the test.

A-type specimens have a characteristic strength of 558 MPa with a 90 % confidence band between 528 MPa and 590 MPa. B-type specimens exhibited characteristic strength of 568 MPa, with the 90 % confidence band between 542 MPa and 595 MPa. Identical characteristic strength values are recorded for C- and D-type specimens and are respectively 528 MPa and 528 MPa. These two specimen types have a similar 90 % confidence band of 500 MPa – 557 MPa and 499 MPa – 560 MPa. In general, the average strength of all specimen types does not vary too much and is within experimental deviation for high-strength, high-purity alumina. This can be attributed to the exposure energy applied during the green body fabrication process. Exposure energy remained nearly constant and the layer thickness was the main variable. Using exposure energy that is too low would cause layer adhesion issues, as shown earlier in this study. Perhaps the sintering process itself is also giving this high consistent average strength.

The highest Weibull modulus of 6.6 was calculated for B-type specimens and C-type specimens exhibited the lowest modulus of 4.9. Fig. 8 shows Weibull diagrams for A-; B-; C- and D-type of the tested specimens.

Schwentenwein *et al.* [19,21] performed mechanical testing of alumina ceramics prepared by means of 3D manufacturing with LCM technology using LithaLox HP500 dispersion on 30 specimens [19]. They fabricated bar specimens for 4-point bending tests. They achieved a strength of 427 MPa and a Weibull modulus of 11.2. Owing to the different tests performed and therefore different specimen dimensions in their study and in ours, the results cannot be directly compared. However, the higher Weibull modulus calculated in their study suggests lower deviation in specimen-to-specimen strength values. In the B3B test, the highest stresses appear on the surface of the tensile side and surface defects have a great influence on the strength and the scatter of data. Therefore, the surface defects may have an influence on the low Weibull modulus values. Some low strength values have a significant impact on the scatter of data, while having a small influence on the characteristic strength.

Some of the specimens examined with the B3B test were further investigated by means of SEM to find possible fracture origins. According to the literature, the maximum tensile stress is located in the center of a specimen [25, 30, 31, 32]. Additionally, a fracture origin may be found in the area close to or at the tensile surface [25]. Therefore, the tensile sides of the broken specimens were investigated intensively to find the possible fracture origin on one piece of the broken specimen and its match on the opposing piece of the specimen. Grain size measured on the as-sintered surface of alumina discs was 5.83 ± 0.90 µm.

Fig. 9 shows images of two matching fracture surfaces of the specimen A-21 with the possible failure origin marked by the grey dash-dot line. It seems that an agglomerate was present in the specimen and was pulled out during specimen failure, leaving a cavity in one of the broken specimen pieces. Inside the cavity, several pores are present as well as some hackle lines propagating from the pores to the specimen bulk. The value of 334 MPa is the failure strength of specimen A-21.

Fig. 10 depicts the fracture surface of specimen C-29. The specimen broke into three pieces and the fracture origin is located on the tensile side, in the center of the specimen. That specimen exhibited a flexural strength of 372 MPa. It is the lowest strength among all C-type specimens. In Fig. 10, a grey dot-dash line is used to mark the possible fracture origin and crack branching is marked by grey dash arrow lines.

The Griffith/Irwin equation was used to calculate the size of the critical defect of the examined specimens *a*:

$$K_{IC} = \sigma \cdot Y \cdot \sqrt{a} \qquad (2)$$

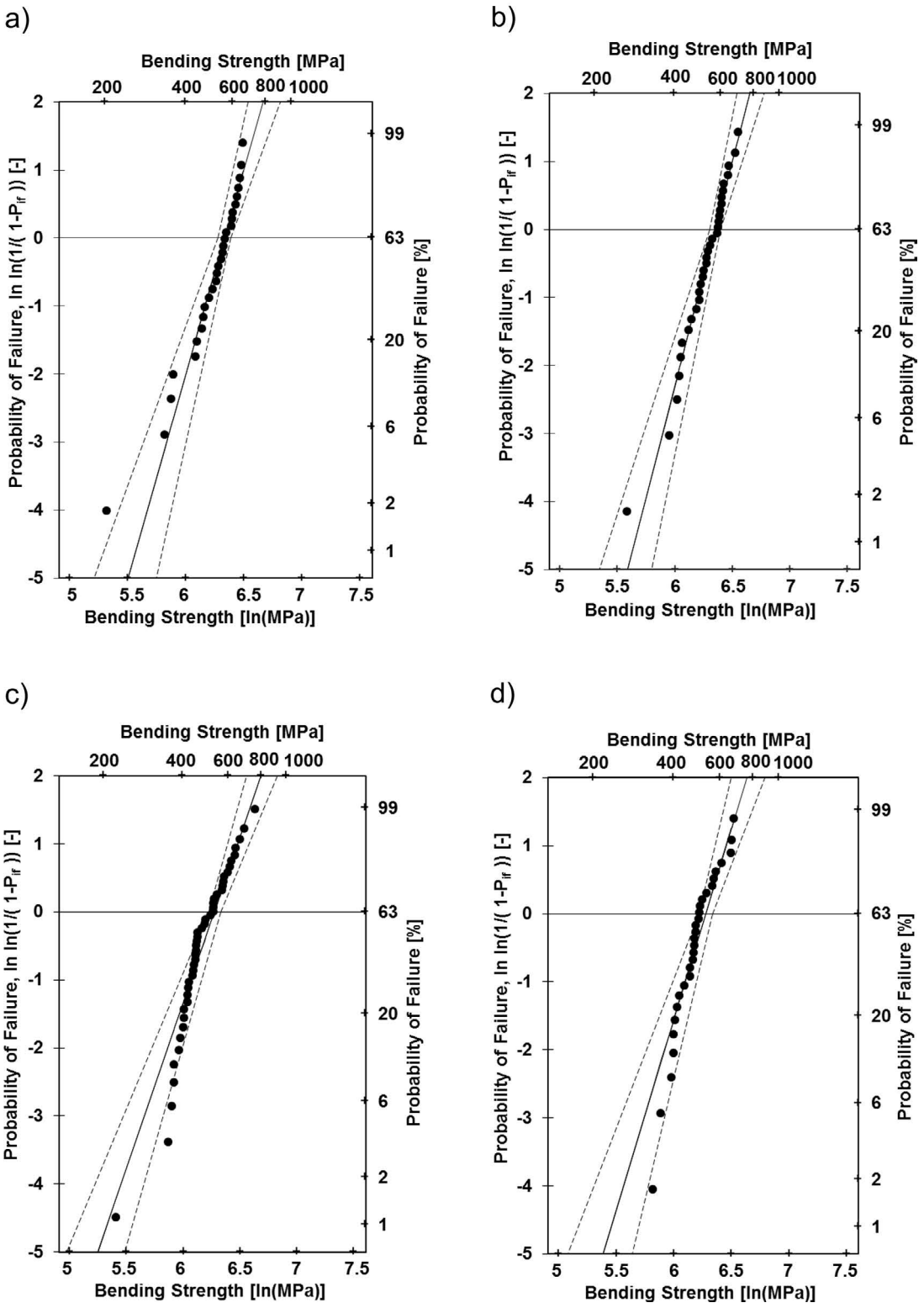

Fig. 8: Weibull probability of failure graphs: a) A; b) B; c) C; and d) D type samples.

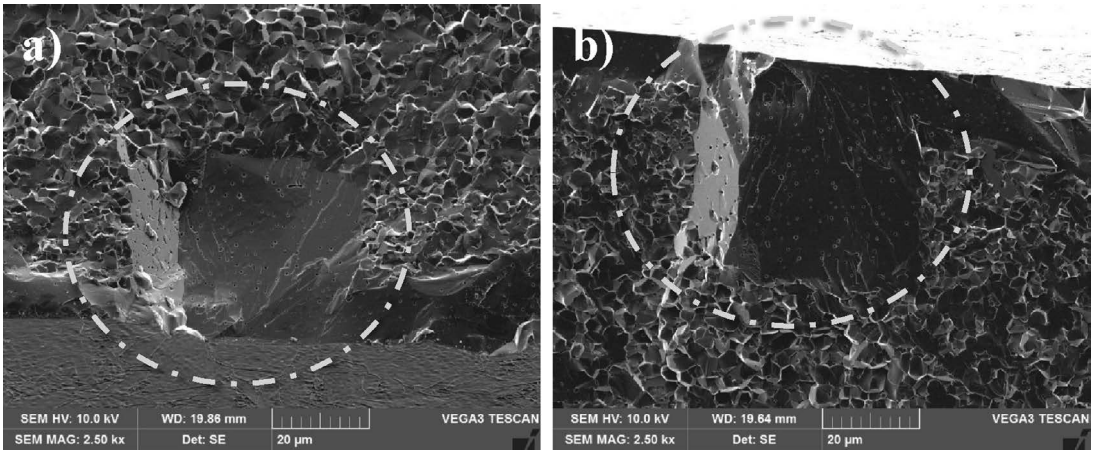

Fig. 9: Fracture origin of the sample A-21: a) a niche after an agglomerate, tensile side on the sample bottom, b) agglomerate, tensile side on the sample top.

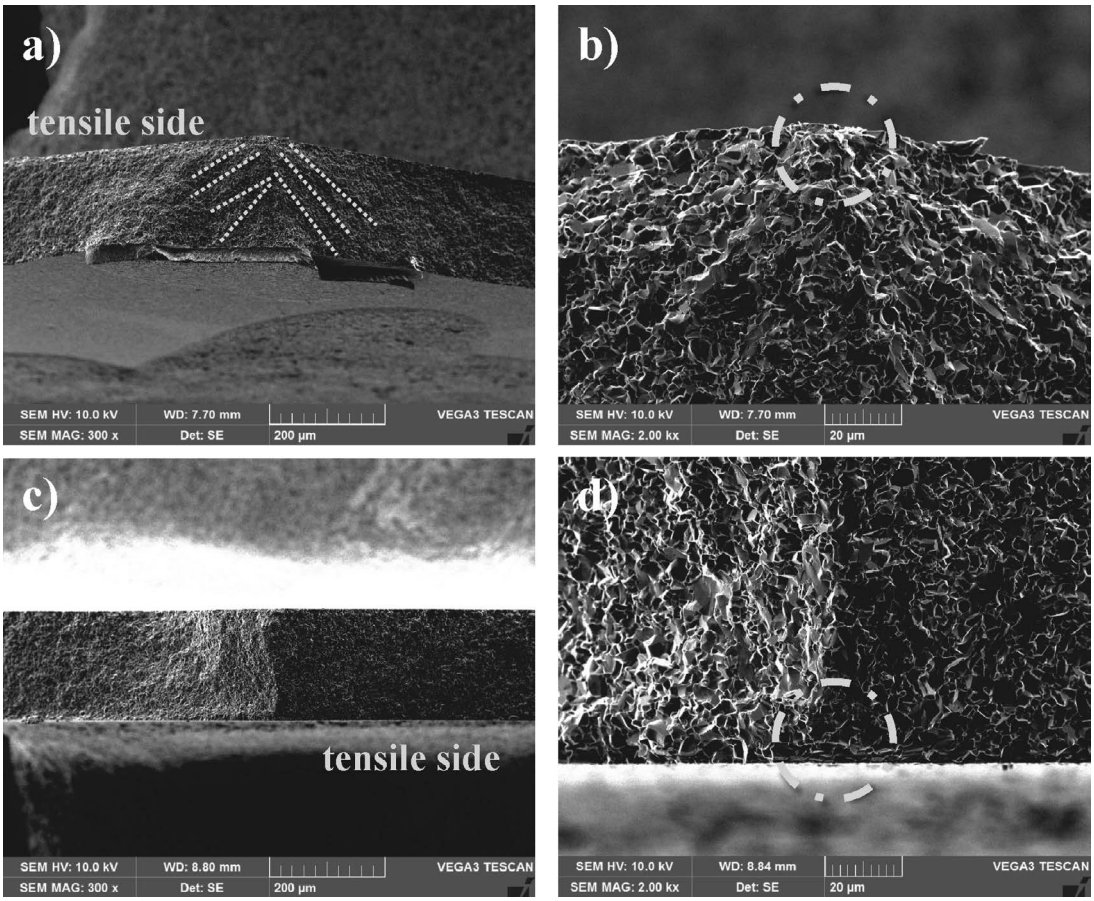

Fig. 10: Fracture surface of the sample C-29 showing possible fracture origin (grey dash-dot line).

$$a = \left(\frac{K_{IC}}{Y \cdot \sigma} \right)^2 \quad (3)$$

where K_{IC} is the fracture toughness [MPa·m$^{0.5}$] for the alumina ceramic, σ is the measured flexural strength [MPa], Y is the geometrical factor for a crack and its value depends on the crack location and shape. The typical K_{IC} value for alumina of 3.5 MPa·m$^{0.5}$ [33] and Y value of 1.29 (for the surface fracture origins) [34] were applied in the calculations. In the case of the specimen A-21, a defect size of 66 µm was calculated. This value is in good agreement with the expected origin size based on the microscopic observations.

This shows that these defects, which are fairly large and consistent, could be eliminated by further optimization of the process. This would lead to higher average strengths of alumina. This shows that the method of forming still has a lot of potential for improvement.

VI. Conclusions

In this study the influence of the printing parameters for LCM 3D shaping technology on the quality of the green bodies and final sintered alumina ceramics was investigated. It has been shown that it is essential to carefully choose the printing parameters used to shape 3-dimensional components free of defects. Reduction in the exposure energy allowed an improvement in *x-y* resolution as it reduces

overgrowth of the polymerized dispersion caused by light scattering. However, exposure energy that is too low will cause delamination of the layers, leading to crack formation in the sintered ceramics. The same phenomenon is observed if a layer thickness that is too high is used in the fabrication process. This necessitates exact and accurate visual investigation of the printed components, both in the green state and after sintering. Such an investigation will be helpful in recognizing defects introduced already at the shaping stage, eliminating them and minimizing the risk of the failure of sintered ceramics. Using different layer thickness does not have any significant impact on the sintered ceramics' average flexural strength if the exposure energy used to solidify the layers is adjusted correctly. We have shown that high-strength alumina ceramics can be produced with this process.

References

1 Halloran, J.W.: Ceramic Stereolithography: additive manufacturing for ceramics by photopolymerization, *Annu. Rev. Mater. Res.*, **46**, [1], 19 – 40, (2016).

2 Zocca, A., Colombo, P., Gomes, C.M., Günster, J.: Additive manufacturing of Ceramics: issues, potentialities, and opportunities, *J. Am. Ceram. Soc.*, **98**, [7], 1983 – 2001, (2015).

3 Ligon, S.C., Liska, R., Stampfl, J., Gurr, M., Mülhaupt, R.: Polymers for 3D printing and customized additive manufacturing, *Chem. Rev.*, **17**, [15], 10212 – 10290, (2017).

4 Deckers, J., Vleugels, J., Kruth, J., Introduction, I.: Additive manufacturing of Ceramics: A review, *J. Ceram. Sci. Technol.*, **5**, [4], 245 – 260, (2014).

5 Wang, W., Yu, H., Liu, Y., Jiang, X., Gao, B.: Trueness analysis of zirconia crowns fabricated with 3-dimensional printing, *J. Prosthet. Dent.*, **121**, [2], 285 – 291, (2019).

6 Azarmi, F., Amiri, A.: Microstructural evolution during fabrication of alumina via laser stereolithography technique, *Ceram. Int.*, **45**, [1], 271 – 278, (2019).

7 Lu, Z.L., Cao, J.W., Jing, H., et al.: Review of main manufacturing processes of complex hollow turbine blades, *Virtual Phys. Prototyp.*, **8**, [2], 87 – 95, (2013).

8 Osman, R.B., Veen, A.J. Van Der, Huiberts, D., Wismeijer, D.: 3D-printing zirconia implants; a dream or a reality? an in-vitro study evaluating the dimensional accuracy, surface topography and mechanical properties of printed zirconia implant and discs, *J. Mech. Behav. Biomed. Mater.*, **75**, 521 – 528, (2017).

9 Romero, A.D.B., Pfaffinger, M., Mitteramskogler, G., Lantada, A.D., Stampfl, J.: Lithography-based additive manufacture of ceramic biodevices with design-controlled surface topographies, *Int. J. Adv. Manuf. Technol.*, 1547 – 1555, (2017).

10 Díaz Lantada, A., de Blas Romero, A., Schwentenwein, M., Jellinek, C., Homa, J., García-Ruíz, J.P.: Monolithic 3D labs-and organs-on-chips obtained by lithography-based ceramic manufacture, *Int. J. Adv. Manuf. Technol.*, **93**, [9 – 12], 3371 – 3381, (2017).

11 Johansson, E., Lidström, O., Johansson, J., Lyckfeldt, O., Adolfsson, E.: Influence of resin composition on the defect formation in alumina manufactured by stereolithography, *Materials (Basel).*, **10**, [138], 11, (2017).

12 Zanchetta, E., Cattaldo, M., Franchin, G., et al.: Stereolithography of SiOC ceramic microcomponents, *Adv. Mater.*, **28**, 370 – 376, (2016).

13 Schwarzer, E., Götz, M., Markova, D., Stafford, D., Scheithauer, U., Moritz, T.: Lithography-based ceramic manufacturing (LCM) – viscosity and cleaning as two quality influencing steps in the process chain of printing green parts, *J. Eur. Ceram. Soc.*, **37**, [16], 5329 – 5338, (2017).

14 Schwarzer, E., Holtzhausen, S., Scheithauer, U., *et al.*: Process development for additive manufacturing of functionally graded alumina toughened zirconia components intended for medical implant application, *J. Eur. Ceram. Soc.*, **39**, [2 – 3], 522 – 530, (2019).

15 Lantada, A.D., Romero, A.D.B., Schwentenwein, M., Jellinek, C., Homa, J.: Lithography-based ceramic manufacture (LCM) of auxetic Structures: present capabilities and challenges, *Smart Mater. Struct.*, **25**, [5], 10, (2016).

16 Varghese, G., Moral, M., Castro-garcía, M., *et al.*: Fabrication and characterisation of ceramics via low-cost DLP 3D printing, *Boletín la Soc. Española Cerámica y Vidr.*, **57**, 9 – 18, (2018).

17 Schwentenwein, M., Homa, J.: Additive manufacturing of dense alumina ceramics, *Int. J. Appl. Ceram. Technol.*, **12**, [1], 1 – 7, (2015).

18 Lithoz GmbH: Slurry data sheet LithaLox HP 500.

19 Schwentenwein, M., Schneider, P., Homa, J.: Lithography-based ceramic Manufacturing: A novel technique for additive manufacturing of high-performance ceramics, *Adv. Sci. Technol.*, **88**, 60 – 64, (2014).

20 Lithoz GmbH: Process parameters LithaLox HP500.

21 Wefers, K., Misra, C.: Oxides and hydroxides of aluminum alcoa technical paper No. 19, Revised, 1987(1987).

22 Danzer, R., Harrer, W., Supancic, P., Lube, T., Wang, Z., Börger, A.: The ball on three balls test-strength and failure analysis of different materials, *J. Eur. Ceram. Soc.*, **27**, 1481 – 1485, (2007).

23 Börger, A., Supancic, P., Danzer, R.: The ball on three balls test for strength testing of brittle discs: stress distribution in the disc, *J. Eur. Ceram. Soc.*, **22**, 1425 – 1436, (2002).

24 European Committee for Standarization: DIN EN 843 – 5 Advanced technical ceramics – Mechanical properties of monolithic ceramics at room temperature – Part 5: Statistical analysis, (2006).

25 European Committee for Standarization: BS EN 623 – 3 Advanced technical ceramics — Monolithic ceramics — General and textural properties - Part 3: Determination of grain size and size distribution (characterized by the linear intercept method), (2001).

26 Michálek, M., Michálková, M., Blugan, G., Kuebler, J.: Strength of pure alumina ceramics above 1 GPa, *Ceram. Int.*, **44**, [3], 3255 – 3260, (2018).

27 Mitteramskogler, G., Gmeiner, R., Felzmann, R., *et al.*: Light curing strategies for lithography-based additive manufacturing of customized ceramics, *Addit. Manuf.*, **1**, 110 – 118, (2014).

28 Harrer, W., Danzer, R., Supancic, P., Lube, T.: Influence of the sample size on the results of B3B-tests, *Key Eng. Mater.*, **409**, 176 – 184, (2009).

29 Harrer, W., Schwentenwein, M., Lube, T., Danzer, R.: Fractography of zirconia-specimens made using additive manufacturing (LCM) technology, *J. Eur. Ceram. Soc.*, **37**, [14], 4331 – 4338, (2017).

30 Börger, A., Supancic, P., Danzer, R.: The ball on three balls test for strength testing of brittle discs: part II: analysis of possible errors in the strength determination, *J. Eur. Ceram. Soc.*, **24**, [10 – 11], 2917 – 2928, (2004).

31 Quinn, G.D., Xu, K., Gettings, J.R., Swab, J.: Standard reference material 2100: Fracture toughness of ceramics, (2001).

32 European Committee for Standarization: DIN EN 843 – 6:2009 – 12 Advanced technical ceramics – Mechanical properties of monolithic ceramics at room temperature – Part 6: Guidance for fractographic investigation, (2009).